

# Rethinking Video Tokenization: A Conditioned Diffusion-based Approach

Nianzu Yang<sup>1,†,\*</sup>, Pandeng Li<sup>2,†</sup>, Liming Zhao<sup>2</sup>, Yang Li<sup>1</sup>, Chen-Wei Xie<sup>2</sup>, Yehui Tang<sup>1</sup>,  
Xudong Lu<sup>1</sup>, Zhihang Liu<sup>2</sup>, Yun Zheng<sup>2</sup>, Yu Liu<sup>2</sup>, Junchi Yan<sup>1,§</sup>

<sup>1</sup> School of Artificial Intelligence & School of Computer Science, Shanghai Jiao Tong University

<sup>2</sup> Tongyi Lab, Alibaba Group

## Abstract

Existing video tokenizers typically use the traditional Variational Autoencoder (VAE) architecture for video compression and reconstruction. However, to achieve good performance, its training process often relies on complex multi-stage training tricks that go beyond basic reconstruction loss and KL regularization. Among these tricks, the most challenging is the precise tuning of adversarial training with additional Generative Adversarial Networks (GANs) in the final stage, which can hinder stable convergence. In contrast to GANs, diffusion models offer more stable training processes and can generate higher-quality results. Inspired by these advantages, we propose **CDT**, a novel **C**onditioned **D**iffusion-based video **T**okenizer, that replaces the GAN-based decoder with a conditional causal diffusion model. The encoder compresses spatio-temporal information into compact latents, while the decoder reconstructs videos through a reverse diffusion process conditioned on these latents. During inference, we incorporate a feature cache mechanism to generate videos of arbitrary length while maintaining temporal continuity and adopt sampling acceleration technique to enhance efficiency. Trained using only a basic MSE diffusion loss for reconstruction, along with KL term and LPIPS perceptual loss from scratch, extensive experiments demonstrate that CDT achieves state-of-the-art performance in video reconstruction tasks with just a single-step sampling. Even a scaled-down version of CDT ( $3\times$  inference speedup) still performs comparably with top baselines. Moreover, the latent video generation model trained with CDT also exhibits superior performance. The source code and pretrained weights are available at <https://github.com/ali-vilab/CDT>.

## 1 Introduction

Video tokenizers [Li et al., 2024, et. al., 2025, Tang et al., 2024, Zhao et al., 2024] bypass the prohibitive computational demands of direct pixel-level manipulation [Sullivan et al., 2012] by encoding raw videos into compact latent representations. Therefore, video tokenization has become a cornerstone of efficient video generation [Brooks et al., 2024, Kong et al., 2024, Ma et al., 2024, Wei et al., 2024]. Current video tokenizers are universally grounded in the Variational Autoencoder (VAE) architecture [Kingma and Welling, 2014, Van Den Oord et al., 2017]. Within this architecture, an encoder network, primarily composed of 3D convolutional layers, compresses input videos into compact low-dimensional latent representations. These representations are then upsampled by a deterministic decoder to faithfully reconstruct original videos in the pixel space.

While the training of VAEs inherently relies on a basic reconstruction loss and a KL regularization, these alone are insufficient for developing effective video tokenizers [Lin et al., 2024, Zhao et al.,

† Equal contribution \* Work done as a student researcher at Tongyi Lab § Corresponding author

2024]. Modern tokenizers usually demand multi-stage training [Li et al., 2024, Kong et al., 2024] as well as additional training configurations [Yang et al., 2024, Zheng et al., 2024, Lin et al., 2024] to function effectively. These configurations include perceptual loss [Zhang et al., 2018] for ensuring high-level semantic consistency, 3D GAN (Generative Adversarial Network) adversarial loss [Esser et al., 2021] for maintaining temporal consistency and spatial fidelity, and initialization from pre-trained image VAEs to enhance stable convergence [Chen et al., 2024, Polyak et al., 2024, Zhou et al., 2024]. The integration of GANs [Goodfellow et al., 2020], however, introduces specific challenges. The training process of GANs is inherently unstable and often suffers from issues like mode collapse [Dhariwal and Nichol, 2021], which necessitates precise and labor-intensive hyperparameter tuning to achieve the desired performance. Despite these difficulties, GANs are critical for their ability to significantly improve the overall realism of reconstruction videos. This is evident in models like the state-of-the-art HunyuanVideo-VAE [Kong et al., 2024], which retains adversarial training, even though it has given up using pre-trained image VAEs to initialize parameters, highlighting the indispensable role of GANs in achieving satisfactory results.

Recently, diffusion models [Ho et al., 2020, Song et al., 2021b] have been recognized as a superior alternative to GANs, offering more stable training and generating higher-quality outputs [Dhariwal and Nichol, 2021]. Motivated by this, we set out to explore using diffusion models to overcome the limitations of training decoders with GANs. In this work, as illustrated in Fig. 1, we introduce a novel **Conditioned Diffusion-based video Tokenizer**, entitled **CDT**. Similar to existing video tokenizers, the

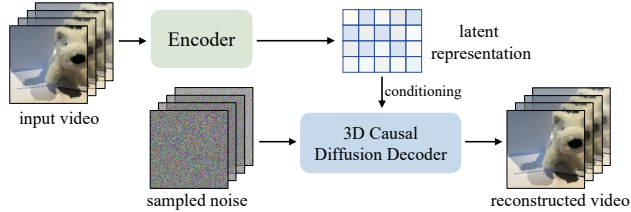


**Figure 1: Overview:** CDT adopts a causal diffusion-based decoder, achieving reconstruction via a reverse diffusion process that is conditioned on the latents extracted by encoder.

encoder in CDT compress input videos into compact latent representation. However, CDT sets itself apart by using a conditional causal diffusion model for decoding, instead of relying on a decoder trained in the GAN fashion. In the decoding phase, the process begins with noise and iteratively refines it through a reverse diffusion process conditioned on the latent representations from the encoder to reconstruct the videos. Our approach simplifies training compared to existing methods by using only the diffusion model’s MSE loss for reconstruction, a KL regularization on the latent space, and an additional LPIPS perceptual loss. To support arbitrary-length video generation and maintain temporal continuity, a feature caching mechanism is incorporated during inference. Moreover, CDT leverages Denoising Diffusion Implicit Model (DDIM) [Song et al., 2021a] for accelerating the diffusion sampling process, enhancing reconstruction efficiency. Extensive experiments demonstrate that CDT achieves state-of-the-art performance in video reconstruction using just a single sampling step. With reduced model parameters, CDT still delivers results comparable to the top baselines. Besides, the latent video generation model built with CDT exhibits superior performance. **Our key contributions are summarized as follows:**

- To the best of our knowledge, we introduce the first diffusion-based video tokenizer without complex training tricks (*e.g.*, multi-stage training with GANs) and hope to shed valuable insights for future research.
- The decoding process is reformulated as a reverse diffusion process conditioned on the latent representations obtained from the encoder to achieve near-exact reconstruction.
- Results show that CDT achieves SOTA reconstruction fidelity via single-step sampling, while also yielding superior performance in latent video generation tasks.

## 2 Preliminaries and Related Works

### 2.1 Diffusion Models

Diffusion models [Ho et al., 2020, Song et al., 2021b] have emerged as a powerful framework for generative modeling, especially in the image and video generation tasks [Nichol et al., 2022, Ho et al., 2022, Croitoru et al., 2023, Esser et al., 2023, Xie et al., 2025]. These models typically comprise two

Markov chains: a forward noising process and a reverse learnable denoising process. The forward process gradually adds noise to a clean data  $\mathbf{x}_0$  over  $T$  timesteps according to a pre-defined variance schedule  $\{\beta_t\}_{t=1}^T$ . At each timestep  $t$ , the transition is defined as:

$$q(\mathbf{x}_t|\mathbf{x}_{t-1}) = \mathcal{N}(\mathbf{x}_t; \sqrt{1 - \beta_t}\mathbf{x}_{t-1}, \beta_t\mathbf{I}). \quad (1)$$

Given this formulation, the state  $\mathbf{x}_t$  at timestep  $t$  can be expressed in a closed-form expression in terms of  $\mathbf{x}_0$  and a noise term  $\epsilon \sim \mathcal{N}(0, \mathbf{I})$ , i.e.,  $\mathbf{x}_t = \sqrt{\bar{\alpha}_t}\mathbf{x}_0 + \sqrt{1 - \bar{\alpha}_t}\epsilon$  where  $\alpha_t = 1 - \beta_t$  and  $\bar{\alpha}_t = \prod_{\tau=1}^t \alpha_\tau$  is the cumulative product of  $\alpha_t$  up to timestep  $t$ . The reverse process begins with  $\mathbf{x}_T$  drawn from the prior distribution. It iteratively removes noise predicted by a neural network  $\epsilon_\theta$  corresponding to the noise injected at the forward timestep, allowing gradually recovering  $\mathbf{x}_0$ . The formulation of the entire denoising process is expressed as  $p_\theta(\mathbf{x}_{0:T}) = p(\mathbf{x}_T) \prod_{t=1}^T p_\theta(\mathbf{x}_{t-1}|\mathbf{x}_t)$ , where  $p_\theta(\mathbf{x}_{t-1}|\mathbf{x}_t)$  is approximated by:

$$p_\theta(\mathbf{x}_{t-1}|\mathbf{x}_t) = \mathcal{N}(\mathbf{x}_{t-1}; \mu_\theta(\mathbf{x}_t, t), \beta_t\mathbf{I}), \quad (2)$$

where  $\mu_\theta(\mathbf{x}_t, t) = \frac{1}{\sqrt{\alpha_t}}\mathbf{x}_t - \frac{\beta_t}{\sqrt{\alpha_t(1-\bar{\alpha}_t)}}\epsilon_\theta(\mathbf{x}_t, t)$  is the predicted posterior mean. The training optimization aims to align  $p_\theta(\mathbf{x}_0)$  with the data distribution  $q(\mathbf{x}_0)$  and the objective adopts the variational upper bound of the negative log-likelihood:

$$\mathcal{L} = \mathbb{E}_q \left[ -\log p_\theta(\mathbf{x}_0|\mathbf{x}_1) + \sum_{t>1} D_{KL}[q(\mathbf{x}_{t-1}|\mathbf{x}_t, \mathbf{x}_0) \parallel p_\theta(\mathbf{x}_{t-1}|\mathbf{x}_t)] \right] + C. \quad (3)$$

Denoising Diffusion Probabilistic Model (DDPM) [Ho et al., 2020] proposes a simplified objective to train the denoising process parameterized by  $\theta$  by directly matching the predicted noise to the actual perturbations added during the forward process, which is formulated as follows:

$$\mathcal{L} = \mathbb{E}_{t, \mathbf{x}_0, \epsilon} \|\epsilon - \epsilon_\theta(\mathbf{x}_t, t)\|^2. \quad (4)$$

Diffusion models are often criticized for their inefficiency in sampling, as they require many iterations to generate high-quality samples. To mitigate this limitation, some techniques [Song et al., 2021a, Lu et al., 2022, Liu et al., 2023, Song et al., 2023] have been proposed to enhance sampling efficiency while preserving strong generation quality. Among these, Denoising Diffusion Implicit Model (DDIM) [Song et al., 2021a] stands out as a representative method. Its primary advantage lies in maintaining the original DDPM training framework while enabling deterministic sampling through a redesigned non-Markovian sampling trajectory. This allows DDIM to achieve comparable generation quality to DDPM with orders-of-magnitude fewer steps.

## 2.2 Video Tokenizers

Existing video tokenizers are typically built on the variational autoencoder (VAE) architecture [Kingma and Welling, 2014] and can be divided into two categories: discrete and continuous tokenizers. In this paper, we specifically focus on continuous tokenization methods, which map video data into continuous latent representations. The differences between continuous and discrete tokenizers are further discussed in Appendix A. With our focus established, we proceed to review representative methods. Earlier works [Blattmann et al., 2023, Guo et al., 2024, Chen et al., 2023] propose to directly apply image tokenizers to video data via frame-wise compression. However, these methods overlook temporal redundancies across frames. The emergence of OpenAI’s Sora has catalyzed [Brooks et al., 2024] some works [Zheng et al., 2024, Lin et al., 2024, Li et al., 2024, et. al., 2025, Zhao et al., 2024, Yang et al., 2024, Kong et al., 2024] aimed at training tokenizers specifically tailored for videos to achieve temporal compression. Among them, OpenSora [Zheng et al., 2024] and OpenSoraPlan [Zheng et al., 2024] stand out as two open-source projects dedicated to re-implementing Sora-like video generative models and they both devise continuous tokenizers for videos to achieve temporal and spatial compression, respectively. CogVideoX [Yang et al., 2024] offers a powerful video VAE with enhanced reconstruction fidelity and, building on this tokenizer, CogVideoX achieves notable text-to-video generation performance. CV-VAE [Zhao et al., 2024] introduces a latent space regularization to ensure its learned latent space is compatible with that of a given image VAE, allowing efficient video model training using pre-trained text-to-image or video models in a spatio-temporally compressed latent space. More recently, HunyuanVideo [Kong et al., 2024] releases a powerful video VAE that delivers new state-of-the-art performance in both image and video reconstruction.

### 3 Methodology

This section is organized as follows: Sec. 3.1 introduces key notations and formally states the problem; Sec. 3.2 formulates our proposed CDT, focusing on its design principles and key ideas; Sec. 3.3 details the implementation of CDT.

#### 3.1 Notations

We follow the causal scenario for video representation, where a video is typically denoted as  $\mathbf{V} \in \mathbb{R}^{(1+F) \times H \times W \times 3}$ . Here,  $1 + F$  denotes the total number of frames, each with a height  $H$  and width  $W$  in RGB format. In this setup, the first frame is processed independently as an image for compression purposes, allowing the video tokenizer to effectively handle both image and video tokenization.

In this paper, we focus on the continuous tokenization approach. Our goal is to train a video tokenizer comprising an encoder  $\mathcal{E}$ , which encodes a video into a compact low-dimensional representation  $\mathbf{z}$ , and a decoder  $\mathcal{D}$ , which reconstructs the video from the obtained  $\mathbf{z}$ . Denoting the reconstructed video as  $\hat{\mathbf{V}}$ , this process can be formulated as:

$$\mathbf{z} = \mathcal{E}(\mathbf{V}), \hat{\mathbf{V}} = \mathcal{D}(\mathbf{z}),$$

where  $\mathbf{z} \in \mathbb{R}^{(1+f) \times h \times w \times c}$ . The compression rate is defined as  $\rho_t \times \rho_s \times \rho_c$ , where  $\rho_t = \frac{F}{f}$  and  $\rho_s = \frac{H}{h} = \frac{W}{w}$  are the temporal and spatial compression factors, respectively.

#### 3.2 Method Formulation

Our key innovation lies in introducing a novel decoding mechanism, while our encoder  $\mathcal{E}$ , parameterized by  $\varphi$ , adheres to the design of existing video tokenizers without specific modifications. The encoder compresses a raw input video into a compact latent representation with sufficient expressive power. To align with the notation in subsequent discussions on diffusion-related decoding, we denote the raw input video as  $\mathbf{V}_0$ . This process is formally expressed as:

$$\mathbf{z} = \mathcal{E}_\varphi(\mathbf{V}_0). \quad (5)$$

The obtained latent representation  $\mathbf{z}$  is used differently from existing methods, which typically upsample  $\mathbf{z}$  directly to the pixel space for video reconstruction. Instead, we use  $\mathbf{z}$  as the condition for the reverse process in our diffusion-based decoder. In the following, we detail this decoder, implemented within the DDPM [Ho et al., 2020] framework. The forward process, starting from the input video  $\mathbf{V}_0$ , follows the noise injection scheme formulated in Eq. 1, which progressively corrupts the video over  $T$  timesteps. The forward transition at timestep  $t$  is defined as:

$$q(\mathbf{V}_t | \mathbf{V}_{t-1}) = \mathcal{N}(\mathbf{V}_t; \sqrt{1 - \beta_t} \mathbf{V}_{t-1}, \beta_t \mathbf{I}), \quad (6)$$

where we use the cosine scheduler [Nichol and Dhariwal, 2021] for  $\beta_t$ . As for the reverse generative process, the decoder receives the extracted latent  $\mathbf{z}$  as a condition. Based on Eq. 2, the conditioned denoising process can be reformulated as:

$$p_\theta(\mathbf{V}_{t-1} | \mathbf{V}_t, \mathbf{z}) = \mathcal{N}(\mathbf{V}_{t-1}; \mu_\theta(\mathbf{V}_t, \mathbf{z}, t), \beta_t \mathbf{I}), \quad (7)$$

where  $\mu_\theta(\mathbf{V}_t, \mathbf{z}, t)$  is further reparameterized by leveraging a noise prediction network  $\epsilon_\theta$  as follows:

$$\mu_\theta(\mathbf{V}_t, \mathbf{z}, t) = \frac{1}{\sqrt{\alpha_t}} \mathbf{V}_t - \frac{\beta_t}{\sqrt{\alpha_t(1 - \bar{\alpha}_t)}} \epsilon_\theta(\mathbf{V}_t, \mathbf{z}, t). \quad (8)$$

**Training Objective.** For the diffusion-based decoding process, to estimate the reconstruction ability of the decoder, we introduce a simplified objective to train this reverse generative process as proposed by DDPM [Ho et al., 2020], where the loss function is the mean-squared error between the true noise and the predicted noise at each timestep:

$$\mathcal{L}_{\text{diffusion}} = \mathbb{E}_{t, \mathbf{V}_0, \epsilon} \|\epsilon - \epsilon_\theta(\mathbf{V}_t, \mathbf{z}, t)\|^2. \quad (9)$$

The above  $\mathcal{L}_{\text{diffusion}}$  can be further reformulated [Salimans and Ho, 2022] as:

$$\mathcal{L}_{\text{diffusion}} = \mathbb{E}_{t, \mathbf{V}_0, \epsilon} \frac{\bar{\alpha}_t}{1 - \bar{\alpha}_t} \|\mathbf{V}_0 - \mathcal{V}_\theta(\mathbf{V}_t, \mathbf{z}, t)\|^2, \quad (10)$$

---

**Algorithm 1** Reconstruction

---

**Input:** the input video,  $\mathbf{V}_0$ ;  
sequence of  $N$  time points,  $\{\tau_i\}_{i=1}^N$ , s.t.  $\tau_N = T > \tau_{N-1} > \dots > \tau_1 > \tau_0 = 0$ ;  
*# Encode*  
1:  $\mathbf{z} = \mathcal{E}_\varphi(\mathbf{V}_0)$   
*# Sample  $\mathbf{V}_T$  from the a standard normal distribution*  
2:  $\hat{\mathbf{V}}_{\tau_N} = \mathbf{V}_T \sim \mathcal{N}(\mathbf{0}, \mathbf{I})$   
*# Decode*  
3: **for**  $n = N$  **to** 1 **do**  
4:  $\hat{\mathbf{V}}'_0 = \mathcal{V}_\theta(\hat{\mathbf{V}}_{\tau_n}, \mathbf{z}, \tau_n)$   
5:  $\epsilon_\theta = \frac{\hat{\mathbf{V}}_{\tau_n} - \sqrt{\bar{\alpha}_{\tau_n}} \hat{\mathbf{V}}'_0}{\sqrt{1 - \bar{\alpha}_{\tau_n}}}$  } Use DDIM  
6:  $\hat{\mathbf{V}}_{\tau_{n-1}} = \sqrt{\bar{\alpha}_{\tau_{n-1}}} \hat{\mathbf{V}}'_0 + \sqrt{1 - \bar{\alpha}_{\tau_{n-1}}} \epsilon_\theta$   
7: **end for**  
**Output:** the reconstructed video,  $\hat{\mathbf{V}}_0$ ;

---

where  $\mathcal{V}_\theta$  is a learnable network directly predicting the clean data  $\mathbf{V}_0$ . The equivalence between Eq. 9 and Eq. 10 can be easily derived via  $\epsilon_\theta(\mathbf{V}_t, \mathbf{z}, t) = \frac{\mathbf{V}_t - \sqrt{\bar{\alpha}_t} \mathcal{V}_\theta(\mathbf{V}_t, \mathbf{z}, t)}{\sqrt{1 - \bar{\alpha}_t}}$ . In practice, we adopt Eq. 10 to train the reverse diffusion process.

In addition, a KL regularization on the learned latent space is necessary for facilitating generation. We also introduce a widely-used LPIPS loss [Zhang et al., 2018] to improve perceptual quality of reconstructed videos. Therefore, the final training objective is given by:

$$\mathcal{L} = \mathcal{L}_{\text{diffusion}} + \lambda \mathcal{L}_{\text{KL}} + \eta \mathcal{L}_{\text{LPIPS}}, \quad (11)$$

where  $\lambda$  and  $\eta$  are hyper-parameters. We adopt Eq. 11 as objective to jointly train the encoder and decoder from scratch. Notably, this objective is simpler than those used in existing models [Zhao et al., 2024, Li et al., 2024, Kong et al., 2024] as it excludes adversarial loss, leading to more stable training.

**Decoding.** DDPM typically requires hundreds of sampling steps to generate high-quality outputs, with generation time increasing linearly with the number of steps, leading to relatively low sampling efficiency. To address this, we resort to using DDIM [Song et al., 2021a] sampling method for decoding, which is consistent with the same training approach as DDPM. DDIM can generate high-quality outputs with significantly fewer steps, thereby greatly accelerating our decoding. The sampling formulation of DDIM is presented as follows:

$$\mathbf{V}_{t-1} = \sqrt{\bar{\alpha}_{t-1}} \mathcal{V}_\theta(\mathbf{V}_t, \mathbf{z}, t) + \sqrt{1 - \bar{\alpha}_{t-1}} \epsilon_\theta(\mathbf{V}_t, \mathbf{z}, t). \quad (12)$$

The DDIM sampler enables reverse processes with less iteration number than  $T$ . Specifically, DDIM considers a diffusion process defined on a subset  $\{\mathbf{V}_{\tau_1}, \dots, \mathbf{V}_{\tau_N}\}$ , where  $\tau$  is an increasing sub-sequence of  $[1, \dots, T]$  of length  $N$ . Here,  $N$  is exactly the number of sampling steps required for decoding.  $\mathbf{V}_{\tau_{n-1}}$  can be directly derived from  $\mathbf{V}_{\tau_n}$  via:

$$\mathbf{V}_{\tau_{n-1}} = \sqrt{\bar{\alpha}_{\tau_{n-1}}} \mathcal{V}_\theta(\mathbf{V}_{\tau_n}, \mathbf{z}, \tau_n) + \sqrt{1 - \bar{\alpha}_{\tau_{n-1}}} \epsilon_\theta(\mathbf{V}_{\tau_n}, \mathbf{z}, \tau_n). \quad (13)$$

We formalize the reconstruction procedure using DDIM in Alg. 1. With sufficient training, we observe that even a single DDIM sampling step (*i.e.*,  $N = 1$ ) can achieve impressive fidelity with high efficiency. Moreover, increasing the number of sampling steps further enhances reconstruction faithfulness as shown in Sec. 4.5; however, this comes at the expense of efficiency, highlighting an inherent trade-off.

### 3.3 Model Instantiation

We highlight the architecture of CDT in Fig. 2. CDT is implemented as a causal tokenizer because it is based on 3D causal convolutions [Yu et al., 2023], ensuring that each frame only accesses information from preceding frames.

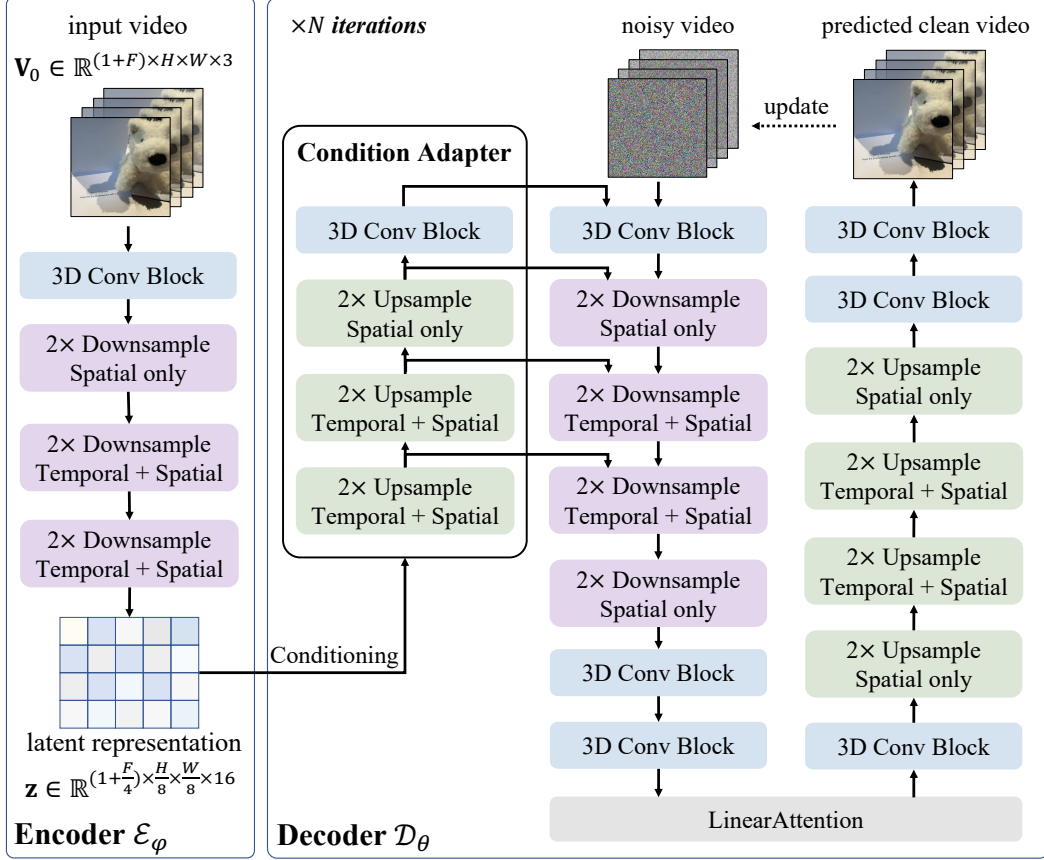


**Figure 2:** The architecture of the proposed CDT.

### 3.3.1 Encoder Implementation

The encoder is responsible for compressing the input video  $\mathbf{V}_0 \in \mathbb{R}^{(1+F) \times H \times W \times 3}$  into a compact latent representation. The encoder begins with a convolution block composed of 3D causal convolution layers to initially encode the input video. Following this, there is a 3D convolution module that applies 2x compression only on the spatial dimensions. Subsequently, it is followed by two modules, each performing 2x compression on both the temporal and spatial dimensions, ultimately outputting the 16-dimensional latent representation  $\mathbf{z} \in \mathbb{R}^{(1+\frac{F}{4}) \times \frac{H}{8} \times \frac{W}{8} \times 16}$ . Consistent with the popular compression rate of current mainstream video tokenizers [Zheng et al., 2024, Lin et al., 2024, Yang et al., 2024, Kong et al., 2024], our encoder ultimately achieves a compression rate of  $4 \times 8 \times 8$ .

### 3.3.2 Decoder Implementation

The decoder functions as a conditioned denoising network. We follow the design of the denoising network implemented in DDPM and DDIM, which employs a U-Net-like architecture. The key difference is that they process images using 2D convolution, whereas we handle videos and thus implement a 3D U-Net architecture using 3D causal convolution as our backbone. Specifically, like U-Net, our denoising network is structured into a downsampling stage followed by an upsampling stage, connected by an attention module in between. As noted in Sec. 3.2, our denoising network directly predicts the clean video. Below, we present how to condition the denoising process on the latent representation  $\mathbf{z}$ .

**Condition Injection.** We draw inspiration from the method introduced by Yang and Mandt for incorporating conditions during the denoising process. In our approach, we inject the condition  $\mathbf{z}$  at the downsampling stage of the 3D U-Net. We design a module called **Condition Adapter**,



**Table 1:** Reconstruction performance comparison results on COCO-Val (image) and Webvid-Val (video) datasets in terms of PSNR, SSIM and LPIPS metrics. All methods share the same  $4 \times 8 \times 8$  compression rate, with their latent representation dimensions being either 4 or 16. The **best**, **second-best**, **third-best** and **fourth-best** results are highlighted, respectively.

Model	Latent Dim.	Comp. Rate	Param. Count	COCO2017-Val			Webvid-Val					
				Resolution: original			Resolution: 256 × 256			Resolution: 720 × 720		
				PSNR ↑	SSIM ↑	LPIPS ↓	PSNR ↑	SSIM ↑	LPIPS ↓	PSNR ↑	SSIM ↑	LPIPS ↓
OpenSora-v1.2	4	$4 \times 8 \times 8$	393M	26.85	0.7523	0.1622	29.84	0.8289	0.1261	36.14	0.9339	0.0711
OpenSoraPlan-v1.2	4	$4 \times 8 \times 8$	239M	25.93	0.7276	0.0935	29.64	0.8372	0.0693	36.07	0.9389	0.0421
WF-VAE	4	$4 \times 8 \times 8$	147M	26.91	0.7620	0.1473	30.30	0.8571	0.0956	37.55	0.9533	0.0370
Cosmos-VAE-CV	16	$4 \times 8 \times 8$	105M	27.83	0.8060	0.1800	31.41	0.8843	0.1168	39.79	0.9687	0.0275
CVVAE-SD3	16	$4 \times 8 \times 8$	182M	29.48	<b>0.8445</b>	<b>0.0581</b>	33.08	0.9157	<b>0.0425</b>	40.02	0.9713	0.0207
CogVideoX-1.5	16	$4 \times 8 \times 8$	216M	<b>29.54</b>	0.8439	<b>0.0594</b>	<b>34.67</b>	<b>0.9390</b>	<b>0.0338</b>	<b>40.69</b>	<b>0.9766</b>	<b>0.0206</b>
HunyuanVideo-VAE	16	$4 \times 8 \times 8$	245M	<b>30.43</b>	<b>0.8673</b>	<b>0.0332</b>	<b>35.15</b>	<b>0.9397</b>	<b>0.0197</b>	<b>42.47</b>	<b>0.9816</b>	<b>0.0126</b>
CDT-S	16	$4 \times 8 \times 8$	121M	<b>30.11</b>	<b>0.8569</b>	0.0664	<b>34.47</b>	<b>0.9294</b>	<b>0.0425</b>	<b>42.55</b>	<b>0.9804</b>	<b>0.0162</b>
CDT-B	16	$4 \times 8 \times 8$	193M	<b>30.48</b>	<b>0.8653</b>	<b>0.0414</b>	<b>36.38</b>	<b>0.9542</b>	<b>0.0195</b>	<b>42.73</b>	<b>0.9829</b>	<b>0.0134</b>

which takes  $\mathbf{z}$  as its input. This module consists of four sequentially connected sub-modules, each corresponding in reverse order to the first four downsampling modules of the 3D U-Net. Each sub-module processes the input through a 3D convolution to produce an output that matches the shape of the input of its corresponding module in the downsampling stage. We inject the condition 4 times here in total, and we discuss the effects of varying the number of injections in Sec. 4.4.

**Solution to Arbitrary-Length Videos Processing.** Recall that we follow the notations used in causal scenarios and our proposed CDT is implemented as a causal video tokenizer as well. To enable memory-efficient encoding and decoding arbitrarily long videos, inspired by audio streaming decoding [Yao et al., 2021], we implement the feature cache mechanism within the 3D causal convolution layer and the Temporal Downsample layer. For an input video with  $1 + F$  frames, it is divided into  $1 + F/4$  chunks, matching the number of latent features. The encoding and decoding operation is conducted on each chunk individually, with each chunk handling up to 4 frames to prevent GPU memory overflow. To maintain temporal continuity between chunks, frame-level feature caches from the preceding chunk are maintained and integrated into the convolution computations of subsequent chunks. In the 3D causal convolution setting, two cached features (convolution kernel size = 3) are maintained, applying zero-padding for the initial chunk and reusing the last two frames from the previous chunk for subsequent caches. For scenarios with  $2 \times$  temporal downsampling (stride = 2), non-initial blocks use a single frame cache to ensure temporal correctness. This feature cache mechanism optimizes memory use and preserves video coherence across chunk boundaries, ensuring effective processing for infinite-length videos. Refer to Appendix B for a visual aid that clarifies the feature cache mechanism.

## 4 Experiments

This section verifies the effectiveness of our proposed CDT through comprehensive comparisons against state-of-the-art baselines. More results can be found in Appendix D.

### 4.1 Experimental Setups

**Datasets for Evaluation.** To ensure a fair comparison of reconstruction performance, we follow CVVAE-SD3 [Zhao et al., 2024] and conduct image and video reconstruction on COCO2017-val [Lin et al., 2014] and Webvid-val [Bain et al., 2021], respectively, to evaluate the model’s ability to capture static and dynamic visual information. In detail, for image reconstruction setup, we maintain the images at their original resolution. For video reconstruction, we assess the methods at two resolutions by resizing and cropping the videos to  $256 \times 256$  and  $720 \times 720$ , extracting 17 frames from each video. For the video generation evaluation, we use the SkyTimelapse [Xiong et al., 2018] dataset, cropping each video to a resolution of  $256 \times 256$  for training.

**Datasets for Training.** We use a hybrid training approach using both image and video data, where YFCC-15M [Thomee et al., 2016] serves as the image dataset, and OpenVid-1M [Nan et al., 2025] along with a private self-collected dataset are used as the video data. We train two different configurations of CDT, denoted as **CDT-S** (Small) and **CDT-B** (Base). CDT-S has 121M parameters, while CDT-B has 193M parameters. Both models have a latent representation dimension of 16. Further training details are provided in Appendix C.

**Baselines.** We compare CDT against following state-of-the-art methods, all sharing the same compression rate of  $4 \times 8 \times 8$  as our CDT: OpenSora-v1.2 [Zheng et al., 2024], OpenSoraPlan-v1.2 [Lin et al., 2024], WF-VAE [Li et al., 2024], Cosmos-VAE-CV [et. al., 2025], CVVAE-SD3 [Zhao et al., 2024], CogVideoX-1.5 [Yang et al., 2024], HunyuanVideo-VAE [Kong et al., 2024].

**Metrics.** For assessing the reconstruction performance of images and videos, we utilize the following metrics: Peak Signal-to-Noise Ratio (**PSNR**), Structural Similarity Index Measure (**SSIM**), and Learned Perceptual Image Patch Similarity (**LPIPS**). For evaluating the video generation quality, we employ the Fréchet Video Distance (**FVD**). Unless otherwise specified, all experiments are run in FP32 precision.

## 4.2 Reconstruction

We evaluate all methods in terms of image and video reconstruction fidelity and efficiency. Our CDT utilizes DDIM for decoding with only one step of sampling in this section.

**Reconstruction Performance Comparison.** Table 1 reports the reconstruction results for all methods on images and videos. We first focus on the performance of CDT-B. Despite using approximately 21.22% fewer parameters compared to the top baseline, HunyuanVideo-VAE, CDT-B achieves comparable results in image reconstruction and significantly outperforms HunyuanVideo-VAE in PSNR. Regarding video reconstruction results, CDT-B exhibits leading performance against all baseline methods at a resolution of  $256 \times 256$ , especially excelling in the PSNR and LPIPS by a notable margin. At the higher resolution of  $720 \times 720$ , CDT-B generally maintains its lead, with the exception of a slight lag in the LPIPS metric compared to HunyuanVideo-VAE.

As for CDT-S, its parameter count is only larger than that of Cosmos-VAE-CV, yet it still achieves impressive results. In the image reconstruction task, CDT-S ranks third in PSNR and SSIM metrics, particularly outperforming CogVideoX-1.5, which has 78.51% more parameters than CDT-S. In the video reconstruction experiments, across both resolutions, CDT-S surpasses all other baselines in all three metrics, except for CogVideoX-1.5 and HunyuanVideo-VAE. It is remarkable that even though OpenSora-v1.2 has 3.25 times the number of parameters compared to CDT-S, CDT-S achieves substantial improvements, with increases of 12.14% and 13.90% in PSNR and SSIM, respectively, and a 59.06% reduction in LPIPS, compared to OpenSora-v1.2. At the  $720 \times 720$  resolution, CDT-S is second only to HunyuanVideo-VAE in PSNR and SSIM, with a very small gap. These results further validate the effectiveness of our approach. Moreover, a comparison between CDT-B and CDT-S reveals performance improvements with increased parameters, highlighting the good scalability of our method.

It’s worth mentioning that the encoder of HunyuanVideo-VAE, which is the best-performing method among the baselines, has 100M parameters, whereas our CDT-B only has 28M parameters, a 72% reduction. CDT-S has even fewer parameters, only 6 million, reducing the count by 94%. With such a relatively small number of parameters, the latent representation may be less expressive than that of HunyuanVideo-VAE, which means more information might be lost during the compression process. However, CDT-B achieves superior reconstruction fidelity at a  $256 \times 256$  resolution, and CDT-S achieves comparable results at a  $720 \times 720$  resolution, further demonstrating the powerful reconstruction capabilities of our causal diffusion-based decoder. Additionally, we also present a qualitative comparison but choose to defer the results to Appendix D.2.

**Table 2:** Comparison results of the reconstruction efficiency.

Precision	Model	Time (s)	
		$256 \times 256$	$720 \times 720$
FP32	HunyuanVideo-VAE	0.530	6.620
	CDT-S	0.194	1.891
	CDT-B	0.610	6.408
BF16	HunyuanVideo-VAE	0.406	4.361
	CDT-S	0.132	1.034
	CDT-B	0.372	3.122

**Efficiency Comparison.** Aside from fidelity, efficiency is also a crucial factor in evaluating the performance of a video tokenizer reconstruction. Here, we focus on comparing the efficiency with HunyuanVideo-VAE, as its overall fidelity ranks the highest among the baselines. While the primary experiments utilize FP32 precision, BF16 precision is also assessed for a more comprehensive comparison in this study. Table 2 summarizes



the average time cost of reconstructing a single video at both resolutions for our method and HunyuanVideo-VAE, under both precision settings. These experiments were conducted on a single A100 GPU with 80GB of memory. In addition to efficiency, we also compare reconstruction fidelity under BF16 precision. The results are provided in Appendix D.1, where our method still achieves superior results. When using BF16 precision, CDT-B consistently outperforms HunyuanVideo-VAE at both resolutions. At the  $720 \times 720$  resolution, our method demonstrates a substantial efficiency advantage, achieving a 28.41% speedup. Furthermore, CDT-B continues to outperform HunyuanVideo-VAE at the  $720 \times 720$  resolution, although there is a slight dip in efficiency at the  $256 \times 256$  resolution. Across both precision settings, CDT-B demonstrates an efficiency advantage at the high resolution. This efficiency gain is attributed to the fact that HunyuanVideo-VAE requires tiling to process high-resolution videos, which involves splitting the video into overlapping tiles for separate processing and then merging the outputs to avoid out-of-memory issues. In contrast, CDT employs a feature cache mechanism as detailed in Sec. 3.3, instead of the tiling strategy, thereby avoiding the associated computational overhead. Furthermore, recalling the results in Table 1, CDT-S achieves PSNR and SSIM results on par with HunyuanVideo-VAE for  $720 \times 720$  resolution videos in FP32 precision, while reducing the time cost by 71.44%. Additionally, at the  $256 \times 256$  resolution, CDT-S also achieves a 63.40% reduction in time cost compared to HunyuanVideo-VAE. Therefore, CDT-S can serve as a powerful tokenizer offering a good trade-off between efficiency and fidelity.

### 4.3 Video Generation

We further conduct experiments to evaluate whether our CDT is effective in the video generation task when combined with the latent diffusion method. Based on the reconstruction results shown in Sec. 4.2, HunyuanVideo-VAE performs the best among all baselines, so we choose to compare directly with HunyuanVideo-VAE only. We adopt the Latte framework [Ma et al., 2024], specifically using Latte-XL/2, to train latent video generation models based on the latent spaces learned by CDT-B and HunyuanVideo-VAE, respectively, on the SkyTimelapse dataset. Each model is trained for a total of 120k steps using  $8 \times$  A100 GPUs with 80GB memory each.

The FVD ( $\downarrow$ ) is calculated every 20k steps. We randomly sample 1k real videos from the dataset and fix these samples; each time, we generate 1k videos to calculate the FVD against these fixed real samples. We visualize the change in FVD as the training steps progress in Fig. 3. Up to the 80k steps, HunyuanVideo-VAE generally outperforms CDT in terms of FVD, except for a brief period at the 40k steps where CDT performs better. Particularly, at the 20k steps, our FVD is much higher than that of HunyuanVideo-VAE. Upon analyzing the 16-dimensional latent representations of the SkyTimelapse dataset encoded by both HunyuanVideo-VAE and CDT, we find that the values in each dimension of the representation encoded by CDT are more concentrated and exhibit lower variance compared to those encoded by HunyuanVideo-VAE. This indicates that our learned latent space for the SkyTimelapse dataset is more compact, making the denoised latent representation more sensitive to errors. At the 20k steps, the latent diffusion model has not yet converged, leading to inaccurate denoising, which might explain why our method has a much higher FVD at this early stage.

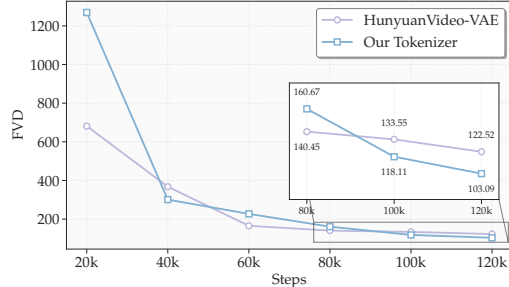
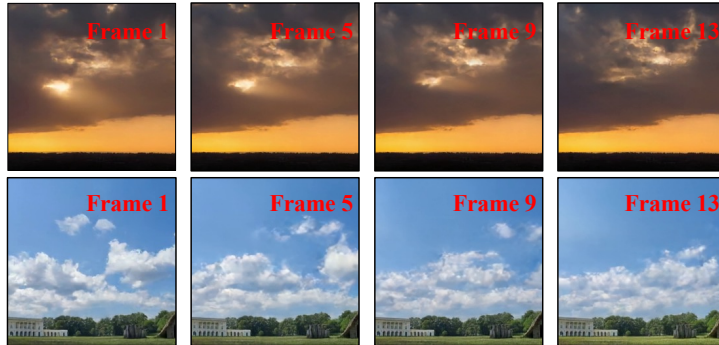


Figure 3: Comparison of FVD trends.

As the steps increase, we see that from the 80k to 100k steps, the FVD of HunyuanVideo-VAE decreases by 4.91%, while during the same period, CDT manages a 26.49% reduction. At the 100k steps, our FVD is 11.56% lower than that of HunyuanVideo-VAE. Continuing training for 20k more steps to 120k, we find that the FVD of the CDT-based model remains 15.86% lower than that of HunyuanVideo-VAE. This indicates that, in the later stages of training, the CDT-based model generates videos of higher quality than those based on HunyuanVideo-VAE, demonstrating that our method is a powerful tokenizer for video generation. In Fig. 4, we present two videos generated by the CDT-based model trained for 120k steps, which appear quite realistic. Particularly, the first

**Table 3:** Ablation study on videos at  $256 \times 256$  resolution.

Model Configuration	Webvid-Val		
	PSNR $\uparrow$	SSIM $\uparrow$	LPIPS $\downarrow$
CDT-S (default model configuration)	32.49	0.9060	0.0539
discard $\mathcal{L}_{\text{LPIPS}}$ for training	31.29	0.8875	0.1050
only inject condition once	31.09	0.8916	0.0642
only inject condition twice	32.08	0.9055	0.0592
only inject condition three times	32.23	0.9057	0.0536

**Figure 4:** Examples of videos generated by Latte using CDT.

row features a video where clouds gradually obscure the sun, causing observable changes in the transmitted light, effectively demonstrating CDT’s ability to generate videos that reflect certain laws of physics.

#### 4.4 Ablation Studies

In this study, we investigate the effects of different components on the final reconstruction performance of our proposed CDT. Due to high computational and time requirements, we use the smaller CDT-S model for analysis. Each model, including all variants and the full version, is trained for 140k steps using  $4 \times 80\text{G A100 GPUs}$  to ensure fair comparison. We evaluate the models on Webvid-Val at  $17 \times 256 \times 256$  resolution, presenting results in Table 3.

**Effect of the  $\mathcal{L}_{\text{LPIPS}}$ .** As noted in Eq. 11, our final training objective consists of three components:  $\mathcal{L}_{\text{diffusion}}$ ,  $\mathcal{L}_{\text{KL}}$ , and an optional term  $\mathcal{L}_{\text{LPIPS}}$ . Here, we investigate the impact of  $\mathcal{L}_{\text{LPIPS}}$  on performance. When this component is omitted, we observe a degradation in performance across all our evaluation metrics: PSNR, SSIM, and LPIPS. The decrease in the LPIPS score is particularly pronounced and expected, as this metric is directly related to the perceptual similarity that  $\mathcal{L}_{\text{LPIPS}}$  aims to improve. Besides, the removal also negatively affects PSNR and SSIM scores, suggesting that  $\mathcal{L}_{\text{LPIPS}}$  contributes to enhancing not only perceptual quality but also the fidelity and structural similarity of the generated outputs.

**Effect of the Condition Injection Times.** As mentioned in Sec. 3.3, in our implementation, we choose to inject the encoded latent representation into the first four modules of the downsampling stage of the denoising network, which adopts a 3D U-Net architecture, to condition the denoising process. Here, we experiment with varying the number of condition injections, comparing injections into just the first one, the first two, the first three, and the first four modules. As shown in Table 3, performance generally improves with more injections across all metrics. More injections typically enhance performance by providing richer conditioning information at multiple stages, thereby enabling the network to perform more accurate denoising. We do not explore more than four injections because it would introduce additional parameters, and since four injections already yield satisfactory results according to our experiments, further increasing the number of injections may not be necessary.

## 4.5 Hyper-parameters Sensitivity

This study investigates the sensitivity of our method to these hyper-parameters: *i)* the timestep number for diffusion training and *ii)* the sampling steps for DDIM method used in decoding. Similar to Sec. 4.4, we evaluate models based on CDT-S on videos at the  $17 \times 256 \times 256$  resolution. Additionally, we also discuss the effect of the latent dimension separately in Appendix D.4.

**Effects of Timestep Number on Diffusion Training.** We set the number of timesteps for diffusion to 8192, whereas most works typically adopt around 1000 timesteps [Ho et al., 2020, Dhariwal and Nichol, 2021, Li et al., 2023]. Here, we compare the effects of using 8192 versus 1024 steps, with each model trained on  $4 \times$  A100 GPUs. Table 4 presents the reconstruction results on Webvid-Val after different numbers of training steps. We can see that the performance of both models generally improves across all metrics as the number of training steps increases. A closer inspection reveals that after 70k training steps, the 8192-step model achieves superior SSIM and LPIPS values compared to the 1024-step model. However, the PSNR metric is better for the 1024-step model. This situation remains the same at 80k steps, with the 1024-step model still outperforming in PSNR while lagging in SSIM and LPIPS. By 90k steps, the 8192-step model surpasses the 1024-step model across all metrics. To ensure that the performance advantage of the model with more timesteps at 90k steps is not just temporary, we conduct additional training for 60k steps and retest at 150k steps. The results show that the model trained with more timesteps consistently outperforms the 1024-step model in the later stages of training.

**Table 4:** Video reconstruction results with 8192 vs. 1024 diffusion timesteps, with **best** results highlighted per row.

Step	1024 diffusion steps			8192 diffusion steps		
	PSNR $\uparrow$	SSIM $\uparrow$	LPIPS $\downarrow$	PSNR $\uparrow$	SSIM $\uparrow$	LPIPS $\downarrow$
@70k	<b>30.63</b>	0.8613	0.0800	30.54	<b>0.8780</b>	<b>0.0675</b>
@80k	<b>31.28</b>	0.8843	0.0690	30.88	<b>0.8864</b>	<b>0.0666</b>
@90k	31.54	0.8897	0.0647	<b>31.67</b>	<b>0.8954</b>	<b>0.0611</b>
@150k	31.69	0.8779	0.0536	<b>32.08</b>	<b>0.9036</b>	<b>0.0520</b>

patterns and enabling faster initial convergence, which boosts early performance metrics. In contrast, models with more timesteps discretize the process into finer intervals, theoretically allowing for more precise noise estimation and higher-quality outputs. Yet, this granularity demands extended training to discern subtle inter-step dependencies and optimize the increased complexity of transitions, causing them to initially lag. Over time, as training progresses, the finer temporal resolution of high-timestep models enables superior noise modeling and detail synthesis, ultimately surpassing their low-timestep counterparts. This highlights a trade-off between training efficiency and ultimate performance.

**Table 5:** Reconstruction fidelity and efficiency with varying DDIM sampling steps on a A100 GPU with 80G memory.

Model	Webvid-Val			
	PSNR $\uparrow$	SSIM $\uparrow$	LPIPS $\downarrow$	Time
CogVideoX-1.5	34.67	0.9390	0.0338	0.695s
HunyuanVideo-VAE	35.15	0.9397	0.0197	0.530s
CDT-S (1-step DDIM)	34.47	0.9294	0.0425	0.194s
CDT-S (2-step DDIM)	34.53	0.9311	0.0422	0.353s
CDT-S (3-step DDIM)	34.72	0.9337	0.0416	0.513s

steps, increased steps will reduce the efficiency of our video tokenizer. Therefore, we need to balance generation quality and efficiency well. We use the time cost of HunyuanVideo-VAE as a reference for the maximum acceptable time cost, given its superior fidelity among the baselines. With three sampling steps, our method’s time cost comes very close to that of HunyuanVideo-VAE, although it is still slightly less. However, with four steps, the time cost would exceed that of HunyuanVideo-VAE. Thus, we limit the sampling steps to  $\{1, 2, 3\}$ . The reconstruction fidelity and time costs on Webvid-Val are summarized in Table 5. This table also includes results from CogVideoX-1.5 and HunyuanVideo-VAE, the two best-performing baselines, for comparison. As shown in Table 5, increasing the DDIM sampling steps improves the reconstruction fidelity of CDT-S across all three

The phenomenon arises from the interplay between timestep granularity and training dynamics in diffusion models, which is rooted in the assumption that time intervals are sufficiently small for more accurate noise estimation in diffusion models. Models with fewer timesteps partition the diffusion process into coarser intervals, simplifying the learning of broad noise-reversal

**Effect of Sampling Steps for Decoding.** In Sec. 4.2, we present the CDT results obtained using one-step DDIM [Song et al., 2021a] sampling during decoding. The original DDIM paper indicates that increasing sampling steps can enhance generation quality. Here, we further investigate the impact of increasing DDIM sampling steps on the performance of CDT. Since decoding time scales linearly with the number of sampling

metrics. Specifically, with only one sampling step, CDT-S is inferior to CogVideoX-1.5 in PSNR. However, with three steps, CDT-S surpasses CogVideoX-1.5 in PSNR. We do not use CDT-B with increased sampling steps in this evaluation because its time cost with a single-step sampling is already very close to that of HunyuanVideo-VAE. Increasing the steps would make its time cost significantly higher than HunyuanVideo-VAE’s. In practical applications, within an acceptable time cost, we can increase sampling steps to enhance reconstruction quality, at the cost of some efficiency.

## 5 Conclusion

We propose CDT, a novel diffusion-based video tokenizer, that adopts a 3D conditional causal diffusion model as the decoder. Without overcomplicated training tricks such as multi-stage training with GANs, we elegantly use a simple MSE diffusion loss to achieve high-quality spatio-temporal compression and reconstruction. Furthermore, to support video reconstruction of arbitrary lengths, a feature cache mechanism is employed, alongside sampling acceleration technique to enhance decoding efficiency. CDT achieves state-of-the-art performance in video reconstruction with single-step sampling, achieves competitive results even with a smaller model, and excels in latent video generation.

## References

- Max Bain, Arsha Nagrani, Gül Varol, and Andrew Zisserman. Frozen in time: A joint video and image encoder for end-to-end retrieval. In *ICCV*, pages 1728–1738, 2021. (Cited on page 7)
- Andreas Blattmann, Tim Dockhorn, Sumith Kulal, Daniel Mendelevitch, Maciej Kilian, Dominik Lorenz, Yam Levi, Zion English, Vikram Voleti, Adam Letts, et al. Stable video diffusion: Scaling latent video diffusion models to large datasets. *arXiv preprint arXiv:2311.15127*, 2023. (Cited on page 3)
- Tim Brooks, Bill Peebles, Connor Holmes, Will DePue, Yufei Guo, Li Jing, David Schnurr, Joe Taylor, Troy Luhman, Eric Luhman, Clarence Ng, Ricky Wang, and Aditya Ramesh. Video generation models as world simulators. 2024. URL <https://openai.com/research/video-generation-models-as-world-simulators>. (Cited on pages 1 and 3)
- Haoxin Chen, Menghan Xia, Yingqing He, Yong Zhang, Xiaodong Cun, Shaoshu Yang, Jinbo Xing, Yaofang Liu, Qifeng Chen, Xintao Wang, et al. Videocrafter1: Open diffusion models for high-quality video generation. *arXiv preprint arXiv:2310.19512*, 2023. (Cited on page 3)
- Liuhan Chen, Zongjian Li, Bin Lin, Bin Zhu, Qian Wang, Shenghai Yuan, Xing Zhou, Xinhua Cheng, and Li Yuan. Od-vae: An omni-dimensional video compressor for improving latent video diffusion model. *arXiv preprint arXiv:2409.01199*, 2024. (Cited on page 2)
- Florinel-Alin Croitoru, Vlad Hondru, Radu Tudor Ionescu, and Mubarak Shah. Diffusion models in vision: A survey. *PAMI*, 45(9):10850–10869, 2023. (Cited on page 2)
- Prafulla Dhariwal and Alexander Nichol. Diffusion models beat gans on image synthesis. volume 34, pages 8780–8794, 2021. (Cited on pages 2 and 11)
- Patrick Esser, Robin Rombach, and Bjorn Ommer. Taming transformers for high-resolution image synthesis. In *CVPR*, pages 12873–12883, 2021. (Cited on page 2)
- Patrick Esser, Johnathan Chiu, Parmida Atighehchian, Jonathan Granskog, and Anastasis Germanidis. Structure and content-guided video synthesis with diffusion models. In *ICCV*, pages 7346–7356, 2023. (Cited on page 2)
- NVIDIA et. al. Cosmos world foundation model platform for physical ai. *arXiv preprint arXiv:2501.03575*, 2025. (Cited on pages 1, 3 and 8)
- Ian Goodfellow, Jean Pouget-Abadie, Mehdi Mirza, Bing Xu, David Warde-Farley, Sherjil Ozair, Aaron Courville, and Yoshua Bengio. Generative adversarial networks. *Communications of the ACM*, 63(11):139–144, 2020. (Cited on page 2)

- Yuwei Guo, Ceyuan Yang, Anyi Rao, Zhengyang Liang, Yaohui Wang, Yu Qiao, Maneesh Agrawala, Dahua Lin, and Bo Dai. Animatediff: Animate your personalized text-to-image diffusion models without specific tuning. In *ICLR*, 2024. URL <https://openreview.net/forum?id=Fx2SbBgcte>. (Cited on page 3)
- Jonathan Ho, Ajay Jain, and Pieter Abbeel. Denoising diffusion probabilistic models. In *NeurIPS*, volume 33, pages 6840–6851, 2020. (Cited on pages 2, 3, 4 and 11)
- Jonathan Ho, Tim Salimans, Alexey Gritsenko, William Chan, Mohammad Norouzi, and David J Fleet. Video diffusion models. *NeurIPS*, 35:8633–8646, 2022. (Cited on page 2)
- Diederik P Kingma and Max Welling. Auto-encoding variational bayes. *stat*, 1050:1, 2014. (Cited on pages 1, 3 and 16)
- Weijie Kong, Qi Tian, Zijian Zhang, Rox Min, Zuozhuo Dai, Jin Zhou, Jiangfeng Xiong, Xin Li, Bo Wu, Jianwei Zhang, et al. Hunyuanvideo: A systematic framework for large video generative models. *arXiv preprint arXiv:2412.03603*, 2024. (Cited on pages 1, 2, 3, 5, 6, 8 and 16)
- Yang Li, Jinpei Guo, Runzhong Wang, and Junchi Yan. T2t: From distribution learning in training to gradient search in testing for combinatorial optimization. In *NeurIPS*, 2023. (Cited on page 11)
- Zongjian Li, Bin Lin, Yang Ye, Liuhan Chen, Xinhua Cheng, Shenghai Yuan, and Li Yuan. Wf-vae: Enhancing video vae by wavelet-driven energy flow for latent video diffusion model. *arXiv preprint arXiv:2411.17459*, 2024. (Cited on pages 1, 2, 3, 5, 8 and 16)
- Bin Lin, Yunyang Ge, Xinhua Cheng, Zongjian Li, Bin Zhu, Shaodong Wang, Xianyi He, Yang Ye, Shenghai Yuan, Liuhan Chen, et al. Open-sora plan: Open-source large video generation model. *arXiv preprint arXiv:2412.00131*, 2024. (Cited on pages 1, 2, 3, 6, 8 and 16)
- Tsung-Yi Lin, Michael Maire, Serge Belongie, James Hays, Pietro Perona, Deva Ramanan, Piotr Dollár, and C Lawrence Zitnick. Microsoft coco: Common objects in context. In *ECCV*, pages 740–755. Springer, 2014. (Cited on page 7)
- Xingchao Liu, Chengyue Gong, and qiang liu. Flow straight and fast: Learning to generate and transfer data with rectified flow. In *ICLR*, 2023. URL <https://openreview.net/forum?id=XVjTT1nw5z>. (Cited on page 3)
- Cheng Lu, Yuhao Zhou, Fan Bao, Jianfei Chen, Chongxuan Li, and Jun Zhu. Dpm-solver: A fast ode solver for diffusion probabilistic model sampling in around 10 steps. In *NeurIPS*, volume 35, pages 5775–5787, 2022. (Cited on page 3)
- Xin Ma, Yaohui Wang, Gengyun Jia, Xinyuan Chen, Ziwei Liu, Yuan-Fang Li, Cunjian Chen, and Yu Qiao. Latte: Latent diffusion transformer for video generation. *arXiv preprint arXiv:2401.03048*, 2024. (Cited on pages 1 and 9)
- Kepan Nan, Rui Xie, Penghao Zhou, Tiehan Fan, Zhenheng Yang, Zhijie Chen, Xiang Li, Jian Yang, and Ying Tai. Openvid-1m: A large-scale high-quality dataset for text-to-video generation. In *ICLR*, 2025. URL <https://openreview.net/forum?id=j7kdXSrISM>. (Cited on page 7)
- Alexander Quinn Nichol and Prafulla Dhariwal. Improved denoising diffusion probabilistic models. In *ICML*, pages 8162–8171. PMLR, 2021. (Cited on page 4)
- Alexander Quinn Nichol, Prafulla Dhariwal, Aditya Ramesh, Pranav Shyam, Pamela Mishkin, Bob McGrew, Ilya Sutskever, and Mark Chen. Glide: Towards photorealistic image generation and editing with text-guided diffusion models. In *ICML*, pages 16784–16804. PMLR, 2022. (Cited on page 2)
- Adam Polyak, Amit Zohar, Andrew Brown, Andros Tjandra, Animesh Sinha, Ann Lee, Apoorv Vyas, Bowen Shi, Chih-Yao Ma, Ching-Yao Chuang, et al. Movie gen: A cast of media foundation models. *arXiv preprint arXiv:2410.13720*, 2024. (Cited on page 2)
- Robin Rombach, Andreas Blattmann, Dominik Lorenz, Patrick Esser, and Björn Ommer. High-resolution image synthesis with latent diffusion models. In *CVPR*, pages 10684–10695, 2022. (Cited on page 16)



- Tim Salimans and Jonathan Ho. Progressive distillation for fast sampling of diffusion models. In *ICLR*, 2022. URL <https://openreview.net/forum?id=TIIdIXIpzhoI>. (Cited on page 4)
- Jiaming Song, Chenlin Meng, and Stefano Ermon. Denoising diffusion implicit models. In *ICLR*, 2021a. URL <https://openreview.net/forum?id=St1giarCHLP>. (Cited on pages 2, 3, 5 and 11)
- Yang Song, Jascha Sohl-Dickstein, Diederik P Kingma, Abhishek Kumar, Stefano Ermon, and Ben Poole. Score-based generative modeling through stochastic differential equations. In *ICLR*, 2021b. URL <https://openreview.net/forum?id=PXTIG12RRHS>. (Cited on page 2)
- Yang Song, Prafulla Dhariwal, Mark Chen, and Ilya Sutskever. Consistency models. In *ICML*, pages 32211–32252. PMLR, 2023. (Cited on page 3)
- Gary J Sullivan, Jens-Rainer Ohm, Woo-Jin Han, and Thomas Wiegand. Overview of the high efficiency video coding (hevc) standard. *TCSVT*, 22(12):1649–1668, 2012. (Cited on page 1)
- Anni Tang, Tianyu He, Junliang Guo, Xinle Cheng, Li Song, and Jiang Bian. Vidtok: A versatile and open-source video tokenizer. *arXiv preprint arXiv:2412.13061*, 2024. (Cited on page 1)
- Bart Thomee, David A Shamma, Gerald Friedland, Benjamin Elizalde, Karl Ni, Douglas Poland, Damian Borth, and Li-Jia Li. Yfcc100m: The new data in multimedia research. *Communications of the ACM*, 59(2):64–73, 2016. (Cited on page 7)
- Aaron Van Den Oord, Oriol Vinyals, et al. Neural discrete representation learning. *NeurIPS*, 30, 2017. (Cited on pages 1 and 16)
- Junke Wang, Yi Jiang, Zehuan Yuan, BINGYUE PENG, Zuxuan Wu, and Yu-Gang Jiang. Omnitokenizer: A joint image-video tokenizer for visual generation. In *NeurIPS*, 2024. URL <https://openreview.net/forum?id=H6C4p8Dir7>. (Cited on page 16)
- Yujie Wei, Shiwei Zhang, Zhiwu Qing, Hangjie Yuan, Zhiheng Liu, Yu Liu, Yingya Zhang, Jingren Zhou, and Hongming Shan. Dreamvideo: Composing your dream videos with customized subject and motion. In *CVPR*, pages 6537–6549, 2024. (Cited on page 1)
- Enze Xie, Junsong Chen, Junyu Chen, Han Cai, Haotian Tang, Yujun Lin, Zhekai Zhang, Muyang Li, Ligeng Zhu, Yao Lu, and Song Han. SANA: Efficient high-resolution text-to-image synthesis with linear diffusion transformers. In *ICLR*, 2025. URL <https://openreview.net/forum?id=N80j1XhtYZ>. (Cited on page 2)
- Wei Xiong, Wenhan Luo, Lin Ma, Wei Liu, and Jiebo Luo. Learning to generate time-lapse videos using multi-stage dynamic generative adversarial networks. In *CVPR*, pages 2364–2373, 2018. (Cited on page 7)
- Wilson Yan, Yunzhi Zhang, Pieter Abbeel, and Aravind Srinivas. Videogpt: Video generation using vq-vae and transformers. *arXiv preprint arXiv:2104.10157*, 2021. (Cited on page 16)
- Ruihan Yang and Stephan Mandt. Lossy image compression with conditional diffusion models. In *NeurIPS*, volume 36, pages 64971–64995, 2023. (Cited on page 6)
- Zhuoyi Yang, Jiayan Teng, Wendi Zheng, Ming Ding, Shiyu Huang, Jiazheng Xu, Yuanming Yang, Wenyi Hong, Xiaohan Zhang, Guanyu Feng, et al. Cogvideox: Text-to-video diffusion models with an expert transformer. *arXiv preprint arXiv:2408.06072*, 2024. (Cited on pages 2, 3, 6, 8 and 16)
- Zhuoyuan Yao, Di Wu, Xiong Wang, Binbin Zhang, Fan Yu, Chao Yang, Zhendong Peng, Xiaoyu Chen, Lei Xie, and Xin Lei. Wenet: Production oriented streaming and non-streaming end-to-end speech recognition toolkit. In *InterSpeech*, 2021. (Cited on page 7)
- Lijun Yu, José Lezama, Nitesh B Gundavarapu, Luca Versari, Kihyuk Sohn, David Minnen, Yong Cheng, Vighnesh Birodkar, Agrim Gupta, Xiuye Gu, et al. Language model beats diffusion-tokenizer is key to visual generation. *arXiv preprint arXiv:2310.05737*, 2023. (Cited on page 5)



- Lijun Yu, Jose Lezama, Nitesh Bharadwaj Gundavarapu, Luca Versari, Kihyuk Sohn, David Minnen, Yong Cheng, Agrim Gupta, Xiuye Gu, Alexander G Hauptmann, Boqing Gong, Ming-Hsuan Yang, Irfan Essa, David A Ross, and Lu Jiang. Language model beats diffusion - tokenizer is key to visual generation. In *ICLR*, 2024. URL <https://openreview.net/forum?id=gzqrANCF4g>. (Cited on page 16)
- Richard Zhang, Phillip Isola, Alexei A Efros, Eli Shechtman, and Oliver Wang. The unreasonable effectiveness of deep features as a perceptual metric. In *CVPR*, pages 586–595, 2018. (Cited on pages 2 and 5)
- Sijie Zhao, Yong Zhang, Xiaodong Cun, Shaoshu Yang, Muyao Niu, Xiaoyu Li, Wenbo Hu, and Ying Shan. CV-VAE: A compatible video VAE for latent generative video models. In *NeurIPS*, 2024. (Cited on pages 1, 3, 5, 7, 8 and 16)
- Zangwei Zheng, Xiangyu Peng, Tianji Yang, Chenhui Shen, Shenggui Li, Hongxin Liu, Yukun Zhou, Tianyi Li, and Yang You. Open-sora: Democratizing efficient video production for all. *arXiv preprint arXiv:2412.20404*, 2024. (Cited on pages 2, 3, 6, 8 and 16)
- Yuan Zhou, Qiuyue Wang, Yuxuan Cai, and Huan Yang. Allegro: Open the black box of commercial-level video generation model. *arXiv preprint arXiv:2410.15458*, 2024. (Cited on page 2)

# Appendix of CDT

## A More Related Works Discussion on Video Tokenization

Existing video tokenizers are typically built on the variational autoencoder (VAE) architecture [Kingma and Welling, 2014] and can be divided into two categories: discrete and continuous tokenizers. Discrete tokenizers [Yan et al., 2021, Yu et al., 2024, Wang et al., 2024] adapt the quantization techniques from discrete image tokenization [Van Den Oord et al., 2017] by mapping video frames into a latent space and quantizing these representations via selecting the nearest vectors from a vector codebook. They are commonly used for autoregressive generation, as they can effectively mitigate error accumulation. In contrast, continuous tokenizers [Zhao et al., 2024, Li et al., 2024, Kong et al., 2024] encode videos into low-dimensional latent representations without quantization and generally exhibit superior reconstruction capabilities than discrete methods. In particular, Latent Video Diffusion Models (LVDMs) [Yang et al., 2024, Zheng et al., 2024, Lin et al., 2024] successfully integrate continuous tokenizers with latent diffusion methods [Rombach et al., 2022], yielding impressive video generation performance.

## B Supplementary Illustration of the Feature Cache Mechanism

This section provides an illustration of the feature cache mechanism in Fig. S1, which is intended to facilitate a deeper understanding of its architecture and functionality, serving as a visual aid to complement the written explanation.

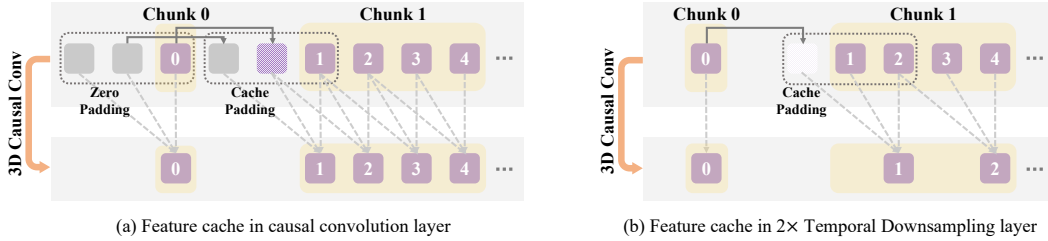


**Figure S1:** Illustration of the architecture and operational flow of the feature cache mechanism.

## C More Training Details of CDT

The training of CDT consists of two stages, primarily differing in the resolution and frame count of the video data. In the first stage, the model is trained on low-resolution videos ( $256 \times 256$ ) with a small number of frames (9 or 17) to accelerate convergence, without introducing the LPIPS perceptual loss. In the second stage, training progresses to videos with higher resolutions (e.g.,  $480 \times 480$  and  $512 \times 512$ ) and a larger number of frames (e.g., 25 and 33), at which point the LPIPS perceptual loss is incorporated with a weighting coefficient of 0.01. The model is trained for a total of 400K steps on 16 Nvidia A100 GPUs. The frame rate (FPS) of all training videos is randomly set between 16 and 60 to facilitate learning across a variety of motion speeds. With this training setup, we obtain the primary configuration of our model, denoted as **CDT-B** (Base), which has 193 million parameters and a latent representation dimension of 16. In addition to the base model, we also train a smaller model, **CDT-S** (Small), with reduced parameters and fewer training steps. CDT-S has 121 million parameters, while still maintaining a latent representation dimension of 16.

## D More Experimental Results

### D.1 Reconstruction Results under BF16 Precision

We present the comparison results of reconstruction performance for various methods on images and videos under BF16 precision in Table S1. It can be observed that performance generally exhibits a slight decline across methods when precision is lowered. Our CDT-B still achieves the

**Table S1:** Reconstruction fidelity comparison results in BF16 precision on COCO-Val and Webvid-Val datasets in terms of PSNR, SSIM and LPIPS metrics. All methods share the same  $4 \times 8 \times 8$  compression rate, with their latent representation dimensions being either 4 or 16. The **best**, **second-best**, **third-best** and **fourth-best** results are highlighted, respectively.

Model	Latent Dim.	Comp. Rate	Param. Count	COCO2017-Val			Webvid-Val					
				Resolution: original			Resolution: $256 \times 256$			Resolution: $720 \times 720$		
				PSNR $\uparrow$	SSIM $\uparrow$	LPIPS $\downarrow$	PSNR $\uparrow$	SSIM $\uparrow$	LPIPS $\downarrow$	PSNR $\uparrow$	SSIM $\uparrow$	LPIPS $\downarrow$
OpenSora-v1.2	4	$4 \times 8 \times 8$	393M	26.83	0.7519	0.1624	29.82	0.8283	0.1263	36.07	0.9335	0.0712
OpenSoraPlan-v1.2	4	$4 \times 8 \times 8$	239M	25.93	0.7274	0.0936	29.64	0.8367	0.0694	36.08	0.9385	0.0421
WF-VAE	4	$4 \times 8 \times 8$	147M	26.89	0.7608	0.1467	30.26	0.8556	0.0955	37.37	0.9513	0.0372
Cosmos-VAE-CV	16	$4 \times 8 \times 8$	105M	27.83	0.8059	0.1801	31.40	0.8842	0.1168	39.79	0.9686	0.0275
CVVAE-SD3	16	$4 \times 8 \times 8$	182M	29.46	<b>0.8443</b>	<b>0.0580</b>	33.04	<b>0.9151</b>	0.0425	40.01	<b>0.9703</b>	0.0207
CogVideoX-1.5	16	$4 \times 8 \times 8$	216M	<b>29.52</b>	0.8440	<b>0.0590</b>	<b>34.65</b>	<b>0.9393</b>	<b>0.0335</b>	<b>40.66</b>	<b>0.9769</b>	<b>0.0204</b>
HunyuanVideo-VAE	16	$4 \times 8 \times 8$	245M	<b>30.42</b>	<b>0.8670</b>	<b>0.0334</b>	<b>35.09</b>	<b>0.9393</b>	<b>0.0198</b>	<b>42.34</b>	<b>0.9810</b>	<b>0.0128</b>
CDT-S	16	$4 \times 8 \times 8$	121M	<b>30.05</b>	<b>0.8555</b>	0.0653	<b>34.32</b>	<b>0.9276</b>	<b>0.0420</b>	<b>42.09</b>	<b>0.9784</b>	<b>0.0160</b>
CDT-B	16	$4 \times 8 \times 8$	193M	<b>30.45</b>	<b>0.8646</b>	<b>0.0414</b>	<b>36.18</b>	<b>0.9526</b>	<b>0.0196</b>	<b>42.29</b>	<b>0.9810</b>	<b>0.0137</b>

best performance across all metrics for video reconstruction at a  $256 \times 256$  resolution. For video reconstruction at a  $720 \times 720$  resolution, it is comparable to HunyuanVideo-VAE. A scaled-down version of our model, i.e., CDT-S, also still demonstrates impressive results at this lower precision. Recalling the comparison provided in Table 2 of the main text under BF16 precision, our method offers a significant efficiency advantage over HunyuanVideo-VAE, while still maintaining a good balance in reconstruction fidelity.

## D.2 Reconstruction Results: A Qualitative Perspective

For a qualitative evaluation, we illustrate some images and videos reconstructed by CDT-S and CDT-B, as well as by other selected baseline tokenizers in this section. We select CVVAE-SD3, CogVideoX-1.5, and HunyuanVideo-VAE for comparison here because these three have the top overall performance among the baselines. Fig. S3 shows several groups of images, each comparing the reconstruction results of different methods on the same image, where it can be observed that our CDT-B method is able to better reconstruct local details. In Fig. S4 and Fig. S5, we present the reconstruction results of one video each. In the example from Fig. S4, our method consistently provides better reconstruction of small text in the video. In the example from Fig. S5, in a video with densely moving people, we can reconstruct dynamic facial details more consistently than other methods. The CDT-S, with even fewer parameters, also achieves good reconstruction results and realism.

## D.3 More Generated Videos by the Model trained in Sec. 4.3

We present more videos generated by the latent video generation model (*i.e.* Latte-XL/2) built upon our CDT-B in Fig. S6. Based on Fig. S6, we can see that the latent video generation trained on the latent space from our CDT is capable of generating diverse and realistic videos, further demonstrating that our proposed conditioned diffusion-based video tokenizer (CDT) can serve as a powerful foundation for video generation.

## D.4 Performance Sensitivity to the Latent Dimension

In this study, we examine how the dimension of latent representation affects the performance of our proposed video tokenizer. Similar to the experiments regarding hyper-parameter sensitivities in the main paper, we continue to evaluate models based on CDT-S. Images are evaluated at their original resolution, while videos are evaluated at a resolution of  $17 \times 256 \times 256$ . By using the CDT-S model configuration, we vary only the latent representation dimension with values of  $\{4, 8, 16\}$ . Each model is trained for 100k steps using four A100 GPUs. The results for image and video reconstruction are shown in Fig. S2. The model with a latent dimension of 16 perform best across all metrics for both image and video data, while the model with a dimension of 8 consistently perform second best. We can observe a strong positive correlation between our method’s reconstruction performance and the latent dimension. This correlation likely arises because higher latent dimension allows for more detailed encoding of the data, enabling the model to better capture and reconstruct complex patterns.

## E Notations

We summarize the notations used in this paper in Table S2 to facilitate reading.

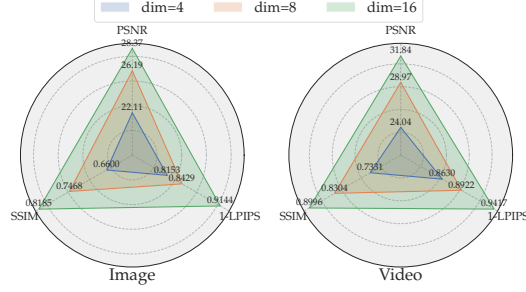


**Figure S2:** Latent dimension impact on the reconstruction performance in terms of PSNR (↑), SSIM (↑), 1-LPIPS (↓).

**Table S2:** Notations.

Notation	Description
$\mathcal{E}$	the encoder of the tokenizer
$\varphi$	learnable parameters for the encoder $\mathcal{E}$
$\mathcal{D}$	the decoder of the tokenizer
$\varphi$	learnable parameters for the decoder $\mathcal{D}$
$\mathbf{z}$	encoded latent representation
$\mathbf{V}$	the input video
$\hat{\mathbf{V}}$	the reconstructed video
$\mathbf{V}_0$	the input clean video in the context of diffusion framework
$\hat{\mathbf{V}}_0$	the predicted clean video
$t$	a specific timestep in the context of diffusion framework
$T$	the total timestep number in the context of diffusion framework
$\beta_t$	the noise scheduler in diffusion
$\alpha_t$	$\alpha_t = 1 - \beta_t$
$\bar{\alpha}_t$	$\bar{\alpha}_t = \prod_{\tau=1}^t \alpha_\tau$
$\epsilon$	injected noise
$\mu_\theta$	the parameterized network for predicting the posterior mean
$\epsilon_\theta$	the parameterized network for predicting the injected noise
$\mathcal{V}_\theta$	the parameterized network for predicting the clean video
$N$	the sampling step number using DDIM in decoding phase

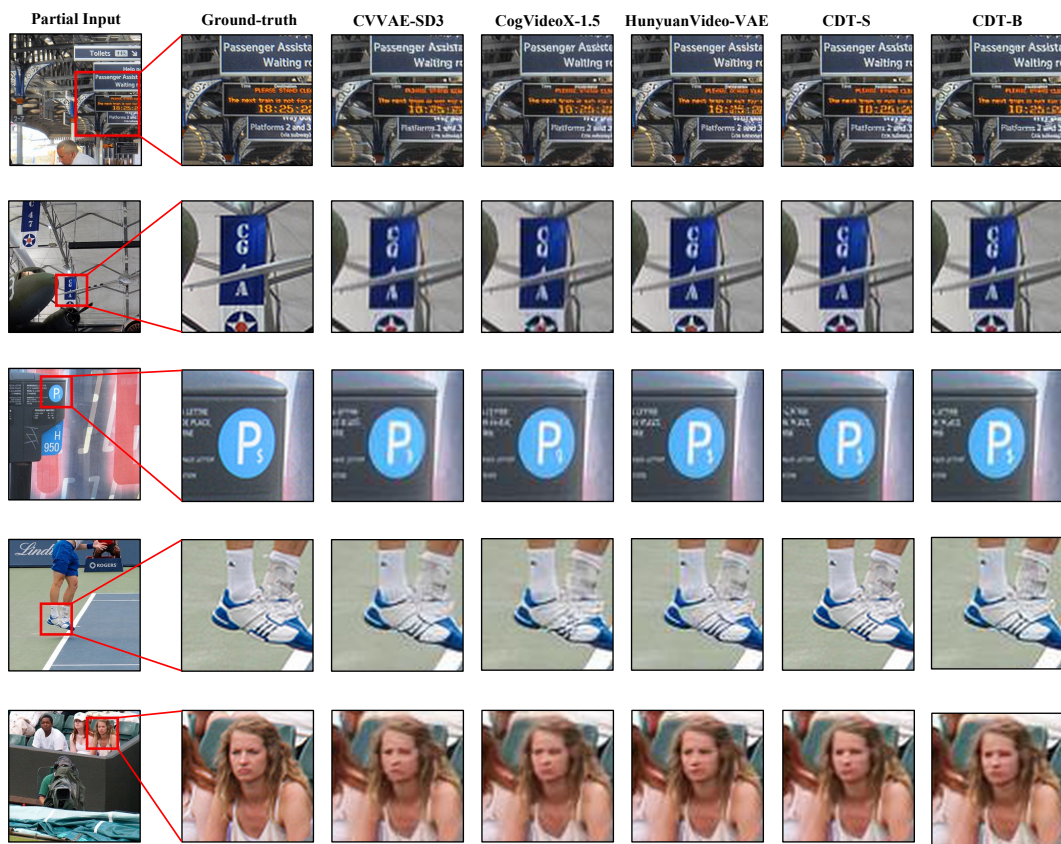


**Figure S3:** Examples of image reconstruction results using different methods, highlighting the superior local detail reconstruction by CDT.



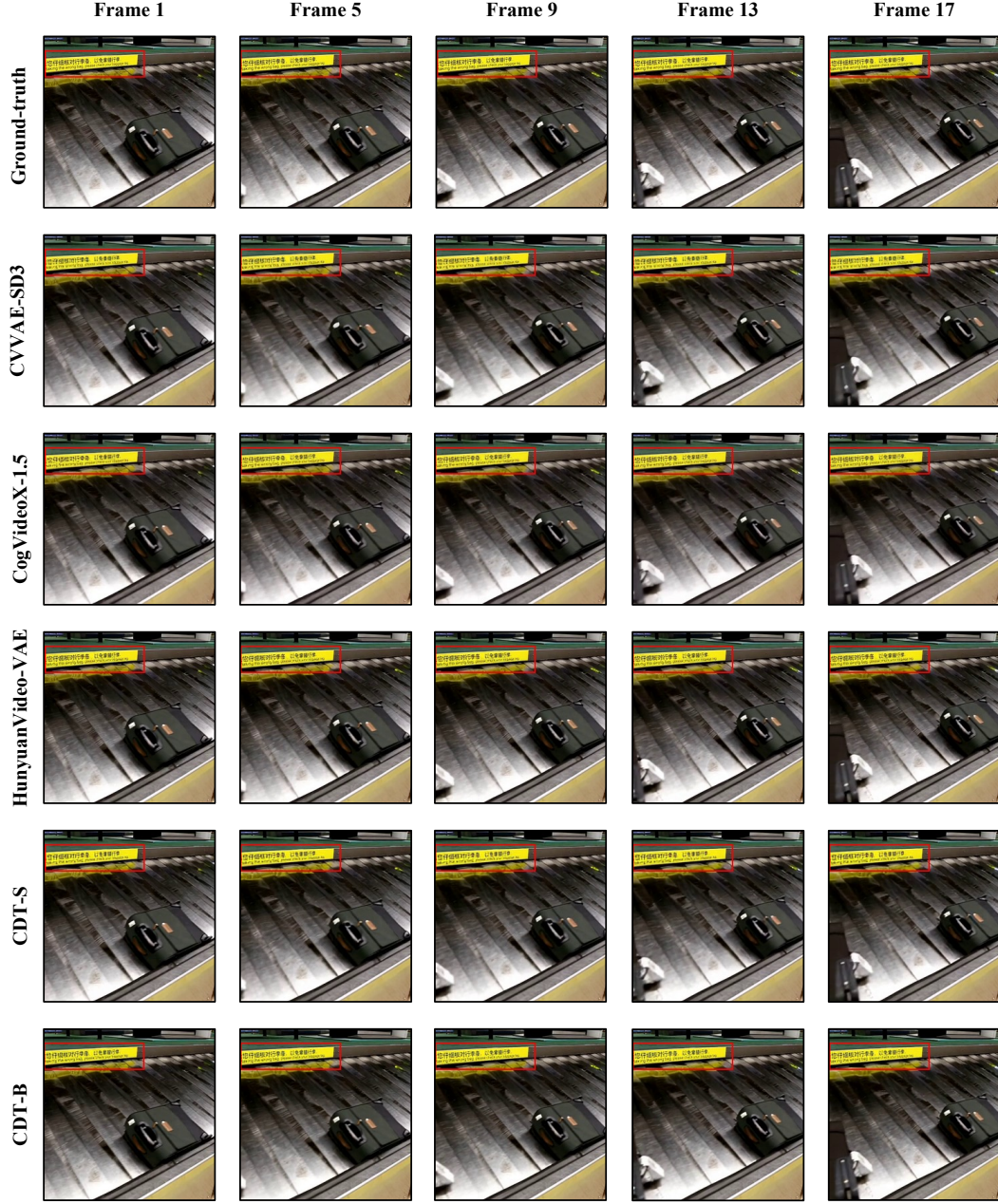


**Figure S4:** Examples of video reconstruction results demonstrating the superior ability of our method to consistently reconstruct small text details.



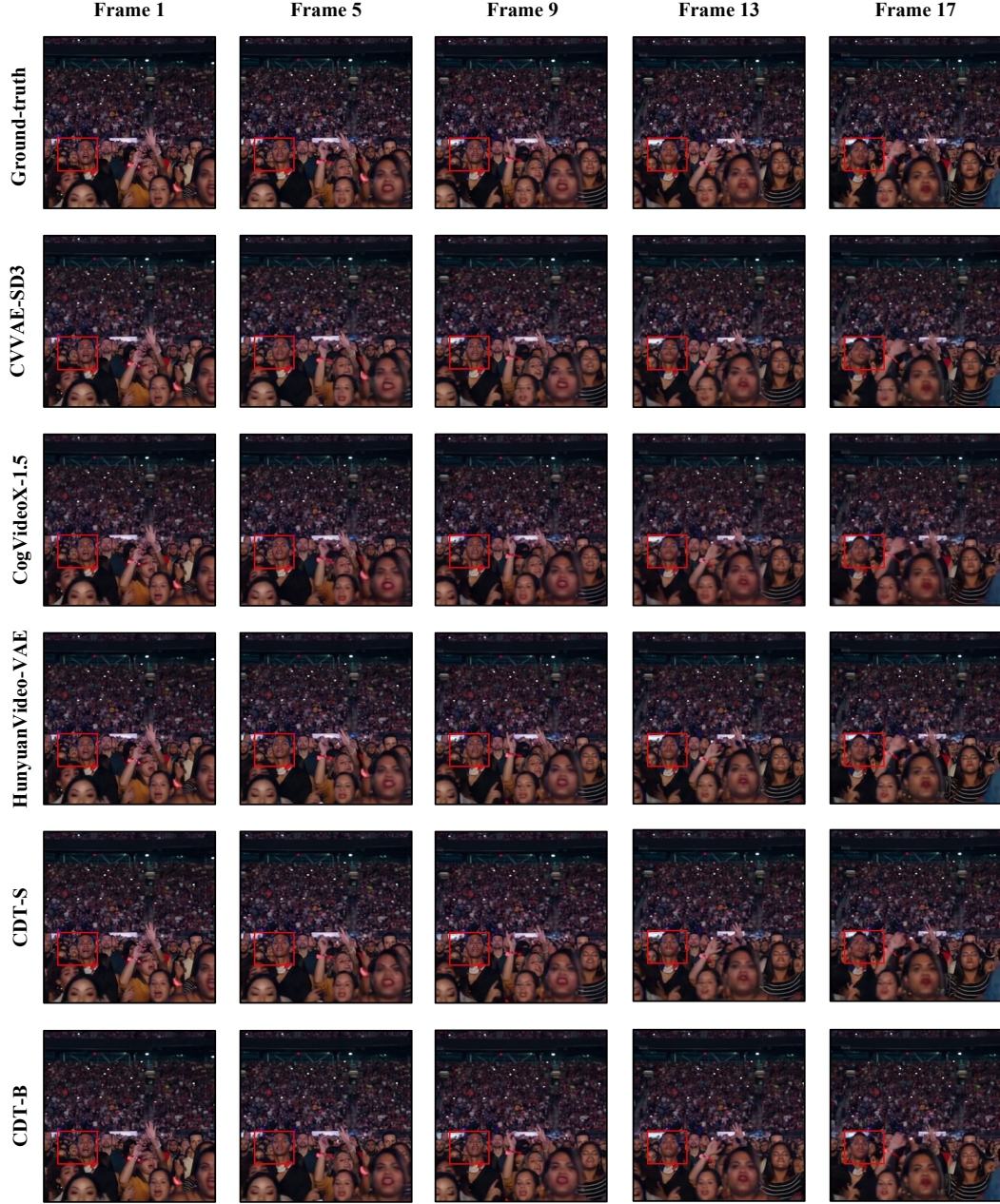


**Figure S5:** Examples of video reconstruction results in a crowded scene, showcasing our method's enhanced ability to consistently reconstruct dynamic facial details.

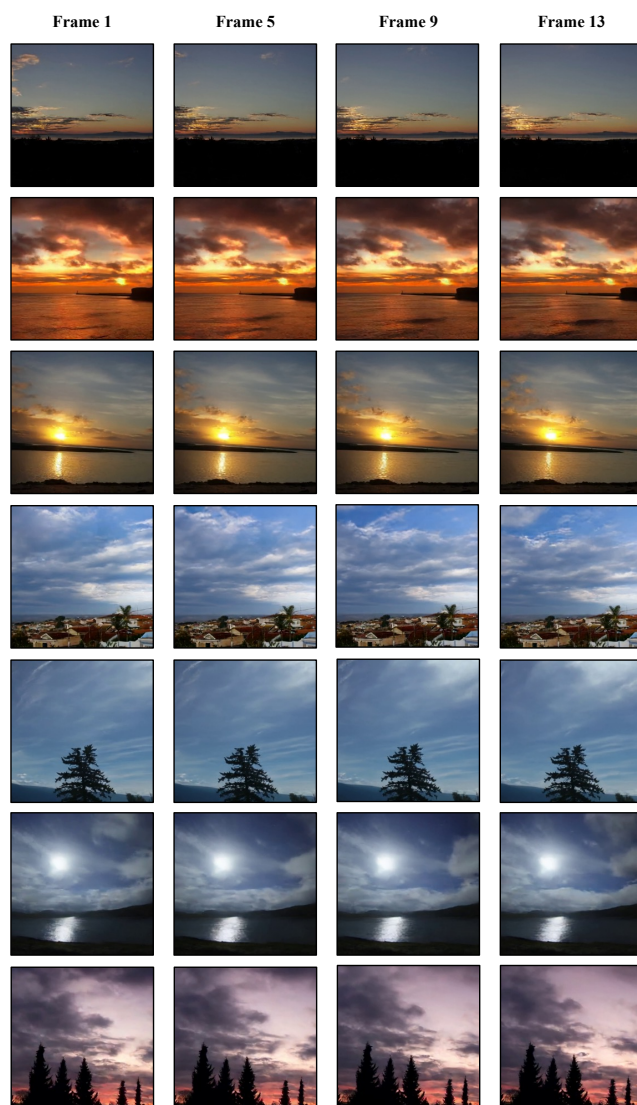


**Figure S6:** More video examples generated by Latte-XL/2 based on CDT-B.